

Monolithically Integrated C-Band Quantum Emitters on Foundry Silicon Photonics

Robert M. Pettit,^{1,*} Skylar Deckoff-Jones,^{1,†} Angela Donis,¹ Ana Elias,¹
Jayson Briscoe,² Gerald Leake,² Daniel Coleman,² Michael Fanto,³ Ananthesh
Sundaresh,¹ Shobhit Gupta,¹ Manish Kumar Singh,¹ and Sean E. Sullivan¹

¹*memQ, Inc, Chicago, IL 60615, USA*

²*State University of New York Polytechnic Institute, Albany, NY 12203, USA*

³*Air Force Research Laboratory, Information Directorate, Rome, NY 13441, USA*

Abstract

Solid-state spin-based quantum systems have emerged as popular platforms for quantum networking applications due to their optical interfaces, their long-lived quantum memories, and their natural compatibility with semiconductor manufacturing. Photonic crystal cavities are often used to enhance radiative emission; however, fabrication of the necessary subwavelength cavities is typically limited to small batch electron beam lithography. In this work, we demonstrate high quality factor, small mode volume nanobeam cavities fabricated on a scalable silicon photonic foundry platform. The foundry fabricated cavities are then interfaced with single erbium ions through backend deposition of TiO_2 thin films lightly doped with erbium. Single ion lifetime measurements indicate Purcell enhancement up to about 500, thereby demonstrating a route toward manufacturable deterministic single photon sources in the telecom C-band.

Networking of different quantum devices using optical fiber and flying qubits is critical for the realization of distributed quantum computing, quantum sensor networks, and secure quantum communication [1–4]. Solid-state spin qubit platforms are particularly appealing for these applications as their spin enables long lived quantum memories and they possess natural optical transitions to coherently convert to photonic qubits [5]. Rare earth ions (REIs) in particular have the additional advantage of long spin coherence and, in the case of trivalent erbium (Er^{3+}), desirable C-band emission for low-loss long-distance fiber propagation. While there have been multiple pioneering works demonstrating isolation and coherent control of individual Er^{3+} ions, these experiments focused on doped bulk crystals (several mm in size) that are not compatible with semiconductor foundry processing [6–9]. Recently it has been shown that REIs can be grown in oxide thin films for monolithic integration with silicon photonics platforms [10–13]. Titanium dioxide (TiO_2) in particular has been demonstrated as a good host material for Er^{3+} ions and is compatible with complementary metal-oxide-semiconductor (CMOS) processing [14]. These films can then be deposited onto silicon-on-insulator (SOI) and patterned into nanophotonic cavities and circuits, where silicon photonic waveguides enable routing and switching and REI optical emission rates are enhanced through the Purcell effect via evanescent coupling to integrated cavities. Using this approach, individual Er^{3+} ions were recently isolated in REI doped

* These authors contributed equally to this work.; robert@memq.tech

† These authors contributed equally to this work.; skylar@memq.tech

oxides on SOI where high Purcell factor-enabling cavities were fabricated through electron beam lithography (EBL) [15].

Subwavelength integrated photonic structures, such as high-Q and small mode volume photonic crystals, are key components to optically interface with solid-state qubits. These structures may also benefit active photonic components such as lasers and modulators due to the devices reduced footprint [16–18]. Traditionally, these devices have been difficult to mass-produce, relying on low-volume methods like EBL. Meanwhile, many commercial integrated photonic foundries, which use the same facilities to fabricate advanced CMOS technology nodes, can now achieve feature sizes below 100 nm. Crucially, the ability to fabricate subwavelength features in the optical layer unlocks wafer-scale and repeatable manufacturing of a new variety of performative and ultra-compact filters, couplers, and cavities [19]. There have been several demonstrations of high-Q photonic crystal-based cavities fabricated on foundry silicon photonics. However, devices are typically not designed with the small mode volumes necessary for Purcell enhancement of quantum emitters [20, 21]. Recently, a demonstration of small mode volume and high-Q suspended 2D photonic crystal cavities was achieved over multiple process optimization runs [22]. Fabrication-robust photonic crystals have also been designed for the particular purpose of interfacing to solid-state qubits, although they have yet to be fabricated on a foundry process [23, 24]. In addition to refinements of critical dimension size via optimized optical lithography, many foundry platforms now offer trenches through the top cladding to the photonic layers meant for evanescent sensing, and these trenches also present the opportunity for backend integration of qubits onto the waveguides.

In this work, we fabricate silicon photonic crystal nanobeam cavities using AIM Photonics’ 300 mm silicon photonic platform and characterize the cavities’ local and wafer scale performance variation. In the backend, $\text{Er}^{3+}:\text{TiO}_2$ thin films are deposited on top of exposed cavities through sensing trenches, providing a facile route for the integration of novel materials with a foundry photonic platform. The impact of the thin film on cavity performance is then measured. We further use the nanobeam cavities to enhance optical emission from single Er^{3+} ions through the Purcell effect [25], creating single photon sources in the C-band on a scalable foundry 300 mm wafer platform. In addition, we also fabricate photonic crystal nanobeam cavities in the silicon nitride layer and Bragg filters for pump rejection [26], and their performance is presented in the Supporting Information.

The devices were fabricated on AIM Photonics’ Quantum Flex (QFlex) 300mm PIC platform. The photonic crystal nanobeam cavities comprise two photonic crystal mirrors defined by holes etched into a silicon waveguide to create a photonic bandgap in the telecom C-band as shown in Fig 1a. In between the mirrors, the pitch of the holes are reduced parabolically to create a resonant midgap state[27]. Figure 1b shows the simulated field intensity of the resonant mode in the silicon cavity, which achieves a small mode volume $< 0.4 (\lambda/n)^3$ due to the high index contrast between silicon and the silicon dioxide cladding. A bus waveguide is then run adjacent to the cavity, where the size of the gap between the bus waveguide and the cavity determines the cavity coupling. Device parameters such as hole size, waveguide width, and coupling gap are varied to optimize device coupling, resonant wavelength, and quality factor. One end of the coupling waveguide goes to an integrated Sagnac loop mirror, while the other end goes to an edge coupler. The devices are characterized in a reflection configuration using a circulator. A reflection spectrum of a silicon cavity is shown in Fig. 1c with a fit to a Lorentzian line shape giving a quality factor of 158,046(30). The best performing silicon cavities achieved quality factors in excess of 150,000.

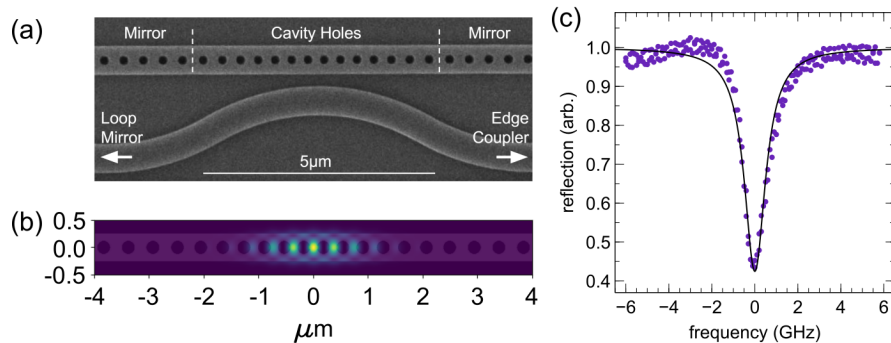


FIG. 1. (a) SEM image of fabricated photonic crystal nanobeam cavity. (b) Simulated optical field intensity in the silicon nanobeam cavity. (c) Reflection spectrum of the silicon nanobeam cavity fit with a Lorentzian line shape to determine the quality factor.

More than 5,000 devices with varying design parameters were characterized using an automated probe station, enabling correlation between design parameters and performance. Fig. 2a shows the silicon cavities resonant wavelength as a function of cavity hole diameter. As the hole diameter is reduced, the resonant wavelength redshifts linearly, creating a

convenient way to control the cavity’s resonant wavelength. For a given hole size, there is still a relatively large distribution, with an interquartile range of >5 nm, because the cavities are extremely sensitive to fabrication variation. Fig. 2b shows the quality factor of cavities as a function of coupling gap size between the bus waveguide and the cavity. The maximum quality factors increase with coupling gap size as the higher Q cavities become critically coupled for larger gap sizes. The minimum quality factors remain similar as some cavities remain overcoupled or undercoupled for a given gap size. The largest measured quality factors were found for devices with the largest gap sizes where they were near critically coupled. Many of the device variations here included trenches through the oxide top cladding to the silicon nanobeam cavities, enabling back-end processing of other materials onto the cavities - CMOS compatible $\text{Er}^{3+}:\text{TiO}_2$ in this case [13, 15]. Device performance from different reticles across the wafer was also characterized, and showed similar performance with a slight radial dependence (see Supporting Information).

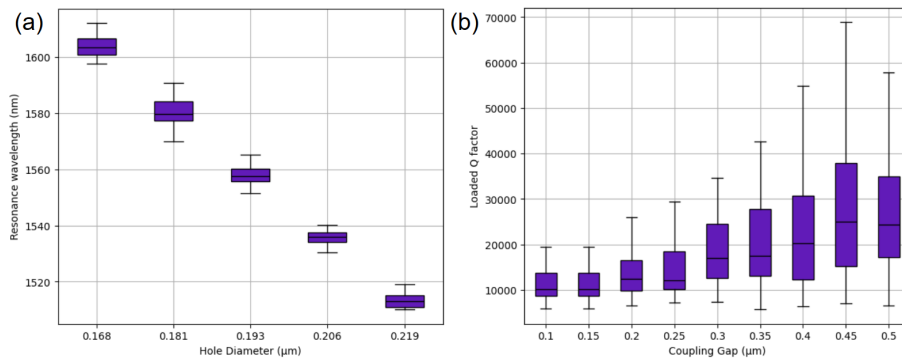


FIG. 2. (a) Box and whisker plot (interquartile range and ± 1.5 quartiles) of the cavity resonance wavelength as a function of photonic crystal cavity hole diameter (b) Box and whisker plot of the cavities quality factor as a function of the gap between the bus waveguide and the cavity.

Upon receiving the wafers from AIM Photonics, $\text{Er}^{3+}:\text{TiO}_2$ films were grown on the photonic crystal through trenches down to the silicon optical layer on the PICs, as shown in Fig. 3a. Many silicon photonic foundries offer a trench to the photonic layer which is generally meant for sensing applications. Here we use it as a way to introduce the “quantum layer” post fabrication. This approach demonstrates a simple way to integrate solid-state quantum materials with commercial foundry integrated photonics without complex lithography or alignment. In the future, $\text{Er}^{3+}:\text{TiO}_2$ can be easily introduced as part of the front-end process, as the necessary tools are already present in AIM’s facilities. The

quantum layer consists of two 10 nm buffer layers of TiO_2 with a 1 nm-thick delta-doped layer of Er^{3+} with a concentration of 2 ppm. The film is polyphase, containing both rutile and anatase phases of TiO_2 and has an RMS surface roughness of 2.4 nm as measured by AFM. Following deposition, the devices were remeasured, and it was found that the resonant wavelengths of the cavities uniformly red shifted by 30 nm, as shown in Fig. 3b. The distribution of the resonance wavelengths remained relatively unchanged. The quality factors of the cavities were also compared before and after the addition of the quantum layer, as shown in Fig. 3c. There was a slight reduction in the cavity Q-factor, which might be a result of the film's surface roughness or material absorption; nevertheless, several cavities still had cavity resonances with Q-factors in excess of 100,000.

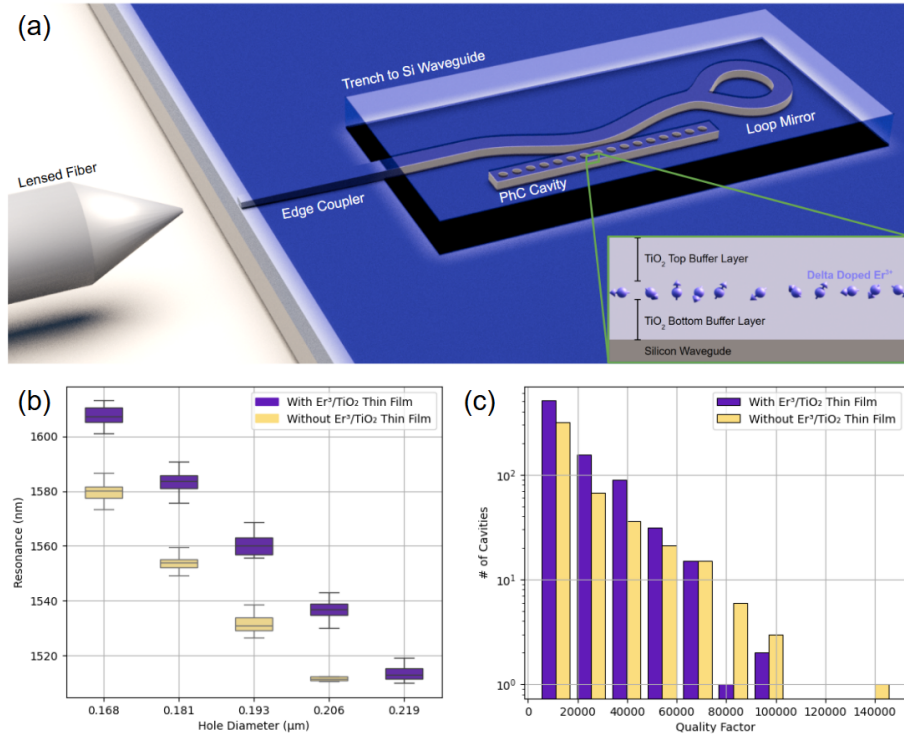


FIG. 3. Portrayal of photonic crystal cavity with trench opening for deposition of quantum layer. The inset shows the cross section of the $\text{Er}^{3+}:\text{TiO}_2$ layer (b) Box and whisker plot (interquartile range and ± 1.5 quartiles) of the cavity resonance wavelength as a function of photonic crystal cavity hole diameter before and after deposition of the $\text{Er}^{3+}:\text{TiO}_2$ layer (c) Histogram of device's Q-factors before and after deposition of the $\text{Er}^{3+}:\text{TiO}_2$ layer.

After room temperature characterization, the sample is placed in a closed-cycle cryostat at $T = 3.4$ K and a lensed optical fiber is aligned to the PIC edge couplers. We perform

photoluminescence excitation (PLE) measurements and observe Er^{3+} ensemble emission in both the rutile and anatase phases near 1520.5 nm and 1532.8 nm respectively, as shown in Fig. 4a. Ensemble emission from the ions is characterized in waveguides without resonant cavities. We observe optical lifetimes of 6.86(44) ns for ions in rutile and 1.61(32) ns for ions in anatase. Our results are consistent with previous investigations of Er^{3+} ensembles in the anatase phase [13] and slightly longer than previous investigations of Er^{3+} ensembles in the rutile phase [11, 14, 28]. We note that TiO_2 is birefringent and the longer lifetime observed here is consistent with the ordinary polarization axis of rutile TiO_2 [14]. In the remainder of this work we focus on the characterization of single ions in the rutile phase. Previous work has investigated single ions in anatase phase TiO_2 , though not on a commercial scale foundry platform [15].

When solid-state quantum emitters are deposited atop the cavities, evanescent coupling of the optical dipoles to the cavity anti-node yields considerable reduction in the radiative lifetime through the Purcell effect [25]. Cavities with resonance wavelengths near 1520.5 nm are tuned through the rutile $\text{Er}^{3+}:\text{TiO}_2$ ensemble emission linewidth by controlled freezing of nitrogen gas onto the cavity [29], enabling the optical isolation of single ions. All single ion measurements shown here are performed with a cavity that has a $Q \sim 37,400$, shown in the Supporting Information. The Purcell enhanced optical lifetime, measured when the ion is resonant with the cavity, is shown in Fig. 4b. The enhanced optical lifetime is found to be $T_1 = 13.80(56) \mu\text{s}$, giving a Purcell factor of $P = 496(38)$ when compared with the emission lifetime of the rutile ensemble in the waveguide.

The optical linewidth of a representative single ion, observed through resonant PLE, is shown in Figure 4c. The ion displays a full width at half maximum linewidth of 57.7 MHz in a single scan fit with a Voigt lineshape with parameters γ , σ as the Lorentzian half width at half maximum and Gaussian standard deviation, respectively. The inhomogeneous contribution to the single scan linewidth is found to be $2\sqrt{2 \ln 2} \sigma = 50.4$ MHz, while the homogeneous contribution is found to be $2\gamma = 13.5$ MHz. Over the course of approximately 2 hours, the ion displays additional slow spectral wandering as shown in the inset. The long-term linewidth over this time span is fully described by its inhomogeneous character and is well fit by a Gaussian lineshape, giving a full width at half maximum of $\Gamma_{\text{inhom}} = 78.8$ MHz. We note that the films studied here have not been optimized in terms of growth and post-growth treatment to achieve narrower emitter linewidths. Further improvements can be achieved

to bring the observed optical linewidths closer to the radiative limit $\Delta\nu_{\text{rad}} = 1/(2\pi T_1)$. Higher Purcell factor cavities can be used to shorten the optical lifetime directly, thereby increasing the radiative linewidth limit. For the results presented here we have not made use of the highest quality factor cavities available on the chip (see Fig. 3c), and higher quality factor cavities should be possible with continued process improvements [22]. An additional route to explore is tailoring the thickness of the thin film buffering layers to reduce the proximity of the ions to interfaces as well as surface passivation techniques [30]. We also note that the size of grains within the polycrystalline film present an area of optimization, as grain boundaries have been shown to contribute to linewidth broadening in rare-earth doped nanocrystals [31, 32].

Finally, we confirm single photon emission from the ion by measuring antibunching in the photon autocorrelation $g^{(2)}(\tau)$, shown in Fig. 4d. In the measurement we use a shot repetition period $> 4T_1$ to reduce inter-shot correlations. At zero time delay we observe $g^{(2)}(0) = 0.27(4)$, which indicates single photon emission for $g^{(2)}(0) < 0.5$. If we take the independently measured background into account, shown in gray, we note that the zero delay autocorrelation improves to $g^{(2)}(0) = 0.10$. In addition to the observed antibunching at zero delay, we also observe photon bunching for time delays $|\tau| > 0$. In the inset we measure the autocorrelation out to time delays $\tau > 1$ s, which is more than four orders of magnitude greater than the Purcell enhanced emitter lifetime. We see that the value of the autocorrelation returns to the Poissonian limit of $g^{(2)}(\tau) = 1$ after about 100 ms. This bunching effect is characteristic of resonantly excited emitters undergoing spectral diffusion [33, 34]. We find that the bunching correlation displays a non-exponential decay, which we characterize with a stretched exponential function to highlight the deviation from a purely exponential decay. We model the bunching for $|\tau| > 0$ as $g^{(2)}(\tau) = B_0 e^{-(\tau/\tau_B)^n} + 1$, where B_0 is the bunching amplitude, τ_B is the characteristic bunching timescale, and n is a stretching parameter that can take values $0 < n < 1$. Here we find a bunching amplitude of $B_0 = 1.66$, with a characteristic bunching time $\tau_B = 7.3$ ms and a stretching parameter $n = 0.38$. We discuss the form of this fit function in more detail in the Supporting Information. The degree of bunching can be used to estimate the homogeneous linewidth of the emitter relative to the inhomogeneous linewidth over the course of the measurement. In the case of a Gaussian broadening process, evidenced by the Gaussian inhomogeneous linewidth observed here, the

bunching amplitude when the emitter is excited on resonance is given by [33],

$$B_0 = \frac{1}{2\sqrt{\pi \ln 2}} \frac{\Gamma_{\text{inhom}}}{\Gamma_{\text{hom}}} - 1.$$

From the observed bunching amplitude, we can therefore estimate the homogeneous linewidth to be $\Gamma_{\text{hom}} = 10.0$ MHz, which is in reasonable agreement with the estimate determined from single PLE scans shown in Fig 4c.

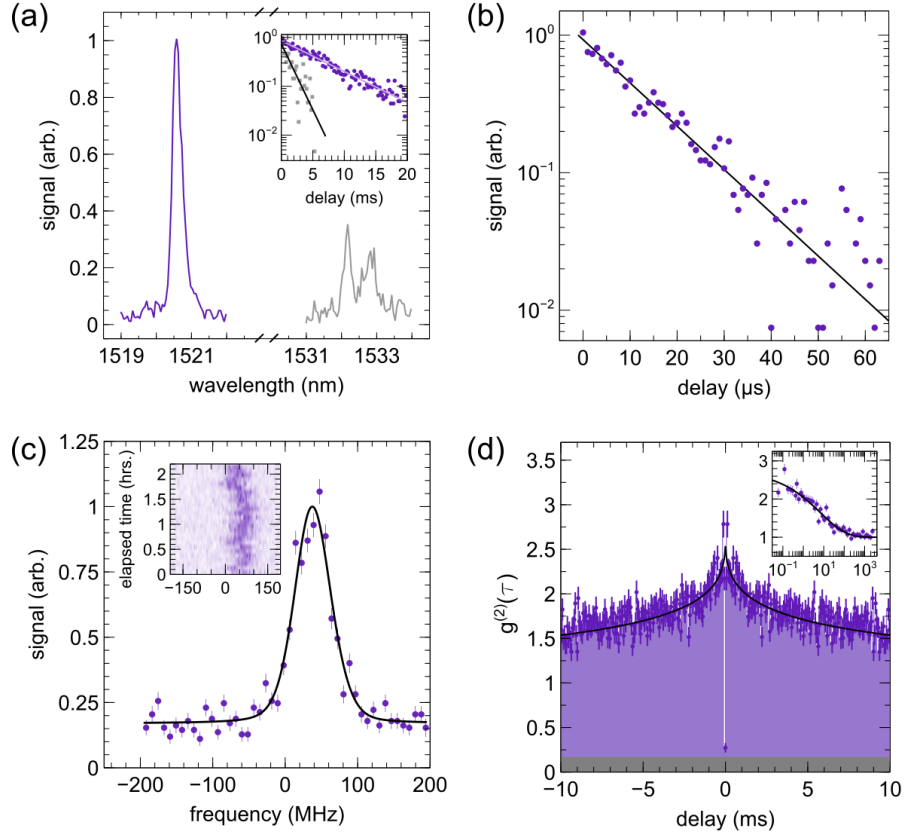


FIG. 4. (a) Photoluminescence excitation of the $\text{Er}^{3+}:\text{TiO}_2$ film showing the inhomogeneous emission from ions in the rutile (purple) and anatase (gray) phases of TiO_2 . Inset: Optical lifetime of Er^{3+} ions in each ensemble measured in an on-chip waveguide. (b) The Purcell enhanced optical lifetime of a single ion in the rutile phase in a resonant cavity. (c) Photoluminescence excitation scan across a single ion in rutile TiO_2 and fit with a Voigt lineshape Inset: Long-term observation of the single ion linewidth for a period > 2 hours. (d) Single photon autocorrelation indicating single photon emission from a single Er^{3+} ion on a silicon nanobeam cavity. Inset: Bunching in the single photon autocorrelation viewed out to a timescale > 1 s.

In conclusion, we have demonstrated silicon photonic crystal cavities on AIM Photonics' Quantum Flex 300 mm platform. We further demonstrated backend deposition of $\text{Er}^{3+}:\text{TiO}_2$ thin films, which offers a scalable approach to developing single-photon emitters with spin-photon interfaces in the telecom C-band. Furthermore, Er^{3+} has been previously demonstrated as an exceptional quantum memory, making this platform ideal for future development of quantum networking systems such as interconnects and quantum repeaters. The results presented here are from post-processing after the wafer left the foundry, although we expect the quality of the roughness and crystallinity to be improved if the material deposition is part of the foundry's process flow, enabling a fully integrated quantum platform. Beyond quantum networking, this work demonstrates that subwavelength photonic devices can be readily fabricated at the foundry level, paving the way for a range of new technologies.

-
- [1] S. Wehner, D. Elkouss, and R. Hanson, Quantum internet: A vision for the road ahead, *Science* **362**, eaam9288 (2018).
 - [2] S.-H. Wei, B. Jing, X.-Y. Zhang, J.-Y. Liao, C.-Z. Yuan, B.-Y. Fan, C. Lyu, D.-L. Zhou, Y. Wang, G.-W. Deng, H.-Z. Song, D. Oblak, G.-C. Guo, and Q. Zhou, Towards Real-World Quantum Networks: A Review, *Laser & Photonics Reviews* **16**, 2100219 (2022).
 - [3] D. Cuomo, M. Caleffi, and A. S. Cacciapuoti, Towards a distributed quantum computing ecosystem, *IET Quantum Communication* **1**, 3 (2020).
 - [4] R. M. Pettit, F. H. Farshi, S. E. Sullivan, Á. Véliz-Osorio, and M. K. Singh, A perspective on the pathway to a scalable quantum internet using rare-earth ions, *Applied Physics Reviews* **10**, 031307 (2023).
 - [5] D. D. Awschalom, R. Hanson, J. Wrachtrup, and B. B. Zhou, Quantum technologies with optically interfaced solid-state spins, *Nature Photon* **12**, 516 (2018).
 - [6] A. M. Dibos, M. Raha, C. M. Phenicie, and J. D. Thompson, Atomic Source of Single Photons in the Telecom Band, *Phys. Rev. Lett.* **120**, 243601 (2018).
 - [7] I. Craiciu, M. Lei, J. Rochman, J. M. Kindem, J. G. Bartholomew, E. Miyazono, T. Zhong, N. Sinclair, and A. Faraon, Nanophotonic Quantum Storage at Telecommunication Wavelength, *Phys. Rev. Appl.* **12**, 024062 (2019).
 - [8] J. M. Kindem, A. Ruskuc, J. G. Bartholomew, J. Rochman, Y. Q. Huan, and A. Faraon,

- Control and single-shot readout of an ion embedded in a nanophotonic cavity, *Nature* **580**, 201 (2020).
- [9] M. Raha, S. Chen, C. M. Phenicie, S. Ourari, A. M. Dibos, and J. D. Thompson, Optical quantum nondemolition measurement of a single rare earth ion qubit, *Nat Commun* **11**, 1605 (2020).
- [10] M. K. Singh, A. Prakash, G. Wolfowicz, J. Wen, Y. Huang, T. Rajh, D. D. Awschalom, T. Zhong, and S. Guha, Epitaxial Er-doped Y_2O_3 on silicon for quantum coherent devices, *APL Materials* **8**, 031111 (2020).
- [11] A. M. Dibos, M. T. Solomon, S. E. Sullivan, M. K. Singh, K. E. Sautter, C. P. Horn, G. D. Grant, Y. Lin, J. Wen, F. J. Heremans, S. Guha, and D. D. Awschalom, Purcell Enhancement of Erbium Ions in TiO_2 on Silicon Nanocavities, *Nano Lett.* **22**, 6530 (2022).
- [12] M. K. Singh, G. D. Grant, G. Wolfowicz, J. Wen, S. E. Sullivan, A. Prakash, A. M. Dibos, F. Joseph Heremans, D. D. Awschalom, and S. Guha, Optical and microstructural studies of erbium-doped TiO_2 thin films on silicon, $SrTiO_3$, and sapphire, *Journal of Applied Physics* **136**, 124402 (2024).
- [13] C. Ji, M. T. Solomon, G. D. Grant, K. Tanaka, M. Hua, J. Wen, S. K. Seth, C. P. Horn, I. Masiulionis, M. K. Singh, S. E. Sullivan, F. J. Heremans, D. D. Awschalom, S. Guha, and A. M. Dibos, Nanocavity-Mediated Purcell Enhancement of Er in TiO_2 Thin Films Grown via Atomic Layer Deposition, *ACS Nano* **18**, 9929 (2024).
- [14] C. M. Phenicie, P. Stevenson, S. Welinski, B. C. Rose, A. T. Asfaw, R. J. Cava, S. A. Lyon, N. P. de Leon, and J. D. Thompson, Narrow Optical Line Widths in Erbium Implanted in TiO_2 , *Nano Lett.* **19**, 8928 (2019).
- [15] C. Ji, R. M. Pettit, S. Gupta, G. D. Grant, I. Masiulionis, A. Sundaresh, S. Deckoff-Jones, M. Olberding, M. K. Singh, F. J. Heremans, S. Guha, A. M. Dibos, and S. E. Sullivan, Isolation of individual Er quantum emitters in anatase TiO_2 on Si photonics, *Applied Physics Letters* **125**, 084001 (2024).
- [16] Y. Zhang, M. Khan, Y. Huang, J. Ryou, P. Deotare, R. Dupuis, and M. Lončar, Photonic crystal nanobeam lasers, *Applied Physics Letters* **97**, 051104 (2010).
- [17] Y. Gong, B. Ellis, G. Shambat, T. Sarmiento, J. S. Harris, and J. Vučković, Nanobeam photonic crystal cavity quantum dot laser, *Optics Express*, Vol. 18, Issue 9, pp. 8781-8789 10.1364/OE.18.008781 (2010).

- [18] H. Zhong, J. Li, Y. He, R. Zhang, H. Wang, J. Shen, Y. Zhang, and Y. Su, Ultra-low-power consumption silicon electro-optic switch based on photonic crystal nanobeam cavity, *npj Nanophoton.* **1**, 1 (2024).
- [19] P. Cheben, R. Halir, J. H. Schmid, H. A. Atwater, and D. R. Smith, Subwavelength integrated photonics, *Nature* **560**, 565 (2018).
- [20] D. Dodane, J. Bourderionnet, S. Combri , and A. De Rossi, Fully embedded photonic crystal cavity with $Q=06$ million fabricated within a full-process CMOS multiproject wafer, *Opt. Express* **26**, 20868 (2018).
- [21] K. P. Arnold, C. S. Whittington, J. A. Allen, S. I. Halimi, F. O. Afzal, Y. Bian, A. Aboketaf, T. Hirokawa, and S. M. Weiss, Deep subwavelength slotted photonic crystal nanobeam in a monolithic silicon photonics foundry, *Opt. Express* **32**, 40350 (2024).
- [22] C. L. Panuski, I. Christen, M. Minkov, C. J. Brabec, S. Trajtenberg-Mills, A. D. Griffiths, J. J. D. McKendry, G. L. Leake, D. J. Coleman, C. Tran, J. St Louis, J. Mucci, C. Horvath, J. N. Westwood-Bachman, S. F. Preble, M. D. Dawson, M. J. Strain, M. L. Fanto, and D. R. Englund, A full degree-of-freedom spatiotemporal light modulator, *Nature Photonics* **16**, 834 (2022), publisher: Nature Publishing Group.
- [23] J. Olthaus, P. P. J. Schrinner, D. E. Reiter, and C. Schuck, Optimal Photonic Crystal Cavities for Coupling Nanoemitters to Photonic Integrated Circuits, *Advanced Quantum Technologies* **3**, 1900084 (2020).
- [24] A. Abulnaga, S. Karg, S. Mukherjee, A. Gupta, K. W. Baldwin, L. N. Pfeiffer, and N. P. de Leon, Design and fabrication of robust hybrid photonic crystal cavities, *Nanophotonics* 10.1515/nanoph-2024-0500 (2024).
- [25] E. M. Purcell, Spontaneous Emission Probabilities at Radio Frequencies, in *Confined Electrons and Photons: New Physics and Applications*, edited by E. Burstein and C. Weisbuch (Springer US, Boston, MA, 1995) pp. 839–839.
- [26] D. Oser, F. Mazeas, X. Le Roux, D. P rez-Galacho, O. Alibart, S. Tanzilli, L. Labont , D. Marris-Morini, L. Vivien,  . Cassan, and C. Alonso-Ramos, Coherency-Broken Bragg Filters: Overcoming On-Chip Rejection Limitations, *Laser & Photonics Reviews* **13**, 1800226 (2019).
- [27] Q. Quan and M. Loncar, Deterministic design of wavelength scale, ultra-high Q photonic crystal nanobeam cavities, *Opt. Express* **19**, 18529 (2011).

- [28] M. T. Solomon, M. Koppenhöfer, M. Mamaev, C. Ji, G. Grant, I. Masiulionis, S. E. Sullivan, F. J. Heremans, S. Guha, D. D. Awschalom, A. A. Clerk, and A. M. Dibos, Anomalous Purcell decay of strongly driven inhomogeneous emitters coupled to a cavity, *Optica Quantum*, OPTICAQ **2**, 196 (2024).
- [29] S. Mosor, J. Hendrickson, B. C. Richards, J. Sweet, G. Khitrova, H. M. Gibbs, T. Yoshie, A. Scherer, O. B. Shchekin, and D. G. Deppe, Scanning a photonic crystal slab nanocavity by condensation of xenon, *Applied Physics Letters* **87**, 141105 (2005).
- [30] J. Liu, K. Konthasinghe, M. Davanço, J. Lawall, V. Anant, V. Verma, R. Mirin, S. W. Nam, J. D. Song, B. Ma, Z. S. Chen, H. Q. Ni, Z. C. Niu, and K. Srinivasan, Single Self-Assembled InAs/GaAs Quantum Dots in Photonic Nanostructures: The Role of Nanofabrication, *Phys. Rev. Appl.* **9**, 064019 (2018).
- [31] J. G. Bartholomew, K. de Oliveira Lima, A. Ferrier, and P. Goldner, Optical Line Width Broadening Mechanisms at the 10 kHz Level in $\text{Eu}^{3+}:\text{Y}_2\text{O}_3$ Nanoparticles, *Nano Lett.* **17**, 778 (2017).
- [32] S. Liu, D. Serrano, A. Fossati, A. Tallaire, A. Ferrier, and P. Goldner, Controlled size reduction of rare earth doped nanoparticles for optical quantum technologies, *RSC Adv.* **8**, 37098 (2018).
- [33] A. Delteil, S. Buil, and J.-P. Hermier, Photon statistics of resonantly driven spectrally diffusive quantum emitters, *Phys. Rev. B* **109**, 155308 (2024).
- [34] G. Sallen, A. Tribu, T. Aichele, R. André, L. Besombes, C. Bougerol, M. Richard, S. Tatarenko, K. Kheng, and J.-P. Poizat, Subnanosecond spectral diffusion measurement using photon correlation, *Nature Photon* **4**, 696 (2010).